

# Blending PHBV with P(3HB-co-4HB) for superior thermal stability, mechanical strength, and environmental degradation†

Ana Carolina Lemos de Moraes,  <sup>a,b</sup> Allef Gabriel da Silva Fortes,  <sup>b</sup> Iago Rodrigues de Abreu,  <sup>b</sup> Corinne van Noordenne-Bos,  <sup>b</sup> Vincent S. D. Voet,  <sup>b</sup> Rudy Folkersma  <sup>b</sup> and Katja Loos  <sup>a,\*</sup>

Received 14th February 2025, Accepted 15th April 2025

DOI: 10.1039/d5fd00035a

Polyhydroxyalkanoates (PHAs) hold significant potential as sustainable alternatives to fossil-based plastics because of their bio-based origin and inherent biodegradability. Poly-3-hydroxybutyrate-co-3-hydroxyvalerate (PHBV) is a well-known commercial member of the PHA family characterized by good mechanical resistance and thermal behavior similar to that of some conventional polymers, such as polypropylene. However, its high crystallinity and fragility limit its application. Poly3-hydroxybutyrate-co-4-hydroxybutyrate (P(3HB-co-4HB)) is a new commercial copolymer containing a 4-hydroxybutyrate (4HB) segment that provides increased flexibility because of its amorphous phase. In this study, PHBV and P(3HB-co-4HB) were blended by extrusion, varying the percentage of P(3HB-co-4HB) to improve the PHBV properties without losing the PHA assets and potentializing the insertion of this biopolymer in the market. The results indicate that the impact energy required for fracture was increased in the polymer blends. These blends exhibited greater thermal stability than pure PHBV, with no significant changes observed in the melting and crystallization temperatures. Furthermore, blending was found to reduce shrinkage in injection-molded samples. The degradation in the soil increased with the highest P(3HB-co-4HB) content. Through 3D printing, it was observed that the blends led to an increase in the melt flow index and a reduction in warpage in the printed objects, thereby facilitating the processing of these materials. Consequently, incorporating P(3HB-co-4HB) into PHBV has emerged as a promising strategy to address the inherent limitations of PHBV. This approach not only enhances the mechanical properties and thermal stability but also improves the overall processability, thereby expanding the potential applications of this biopolymer blend.

<sup>a</sup>Macromolecular Chemistry and New Polymeric Materials, Zernike Institute for Advanced Materials, University of Groningen, Nijenborgh 3, 9747 AG Groningen, The Netherlands. E-mail: [k.u.loos@rug.nl](mailto:k.u.loos@rug.nl)

<sup>b</sup>Circular Plastics, Academy Tech & Design, NHL Stenden University of Applied Sciences, Van Schaikweg 94, 7811 KL Emmen, The Netherlands

† Electronic supplementary information (ESI) available. See DOI: <https://doi.org/10.1039/d5fd00035a>



## Introduction

The polymeric materials industry is responsible for producing over 380 million tons of plastic annually, with an annual growth rate of approximately 4%.<sup>1</sup> A significant portion of these polymers are eventually discarded on land, with a substantial amount subsequently entering marine environments. Notably, around 80% of ocean plastics originate from land-based sources,<sup>1,2</sup> highlighting the critical need for widespread adoption of biodegradable polymers across various industries. Integrating these alternative materials into society is crucial in fields such as agriculture,<sup>3</sup> engineering,<sup>4</sup> health,<sup>5</sup> and packaging.<sup>6</sup>

Polyhydroxyalkanoates (PHAs) are a family of biodegradable polymers naturally produced by various bacterial groups and are classified as natural polyesters. Typically, they exhibit hydrophobic characteristics and are resistant to hydrolytic degradation. While their mechanical properties depend on their chemical structure, PHAs are generally more brittle and have lower elongation at break compared to polypropylene (PP) and polyethylene (PE).<sup>7</sup> Poly(3-hydroxybutyrate-*co*-3-hydroxyvalerate), also known as PHBV, is one of the most common PHA family members.<sup>8,9</sup> Owing to its malleability and ease of processing, this copolymer has been extensively studied and employed across a wide range of applications. Its biocompatibility makes it particularly valuable in the field of biomedicine, while its potential to contribute to the development of environmentally sustainable packaging and electronic materials further underscores its importance.<sup>10,11</sup>

In addition to PHBV, poly(3-hydroxybutyrate-*co*-4-hydroxybutyrate) [P(3HB-*co*-4HB)] is currently recognized as one of the most promising polymers of the PHA family owing to its mechanical properties, including superior elongation at break, as well a range of physical properties from semicrystalline to elastic rubber; it also has noteworthy thermal characteristics, such as its melting point and glass transition, which are adjustable with variation of the amount of 4HB in the copolymer.<sup>12,13</sup> Its inherent biodegradability and biocompatibility further increase its suitability for *in vivo* biomedical applications, making it an excellent candidate for advancing this field.<sup>12,14</sup> In addition, it can be synergistically combined with other polymers to provide better performance properties.<sup>15</sup> Compared with other polymers from the PHA class, P3HB-*co*-4HB has an excellent *in vivo* biodegradation rate in addition to superior elongation at break and tensile strength.<sup>16</sup> The monomers of this copolymer are naturally occurring metabolites in mammals; 3-hydroxybutyrate (3HB) monomers can be found in ketone bodies in the bloodstream, whereas 4-hydroxybutyrate (4HB) monomers can be found in tissue extracts from the brain, heart, and other organs, such as the lungs and kidneys.<sup>17</sup>

Blending processes provide a promising method for enhancing the thermal and mechanical properties of polymers. In particular, blending PHAs with other polymers has proven effective in improving these properties while keeping the overall cost of the final product relatively low. To maintain biodegradability, it is recommended to blend PHAs with other biodegradable polymers, ensuring that the resulting material retains its eco-friendly characteristics. Therefore, it is crucial to select polymers from the same classification to safeguard biodegradability.<sup>18,19</sup> Such combinations may create complementary properties, such as



pairing one polymer with high crystallinity with another having an amorphous structure.

This study developed and assessed blends of PHAs, using PHBV as a matrix, while varying the amount of P(3HB-*co*-4HB) to enhance their mechanical, thermal, and degradability properties. The main goal is to expand the range of potential applications for these materials by employing an easy industrial approach that focuses on improving the PHBV properties, while maintaining its intrinsic identity, with a particular emphasis on their utilization in the fields of packaging disposable plastics. Furthermore, this research highlights the potential to increase the market appeal of PHBV as a sustainable alternative by demonstrating that commercially available PHAs can be effectively utilized through a straightforward methodology to improve their mechanical and thermal properties significantly.

## Experimental

The materials utilized for the production of the polymer blends included PHBV Enmat Y1000P, sourced from TianAn Biologic Materials. This polymer exhibited the following properties: a tensile strength of 39 MPa, a Young's modulus ranging from 2800 to 3500 MPa, and a melting point of 166 °C. Additionally, the study employed PHAx 10007 (PX), a commercial blend consisting of 50% P(3HB-*co*-4HB) and 50% PHBV, in which the P(3HB-*co*-4HB) copolymer consists of 50% 3HB and 50% 4HB, obtained from PHAradox® and supplied by Helian Polymers BV. According to the distributor, this blend possesses a tensile strength of 15 MPa, a Young's modulus of 713 MPa, and a melting point between 150 and 160 °C.

The blends were produced in a two-screw extruder, with an *L/D* of 43 and *D* of 25 mm, from Krauss Maffei Berstorff. Before the blends were produced, all the materials were dried in a vacuum oven at 60 °C for 24 h. A gravimetric feeder type GRAVInet GP controller with Labline feeders from Motan (Colortronic) was used to feed and dose the materials into the extruder. The rotational speed of the screws was set at 300 rpm, and the temperatures used were 45, 150, 190, 180, 180, 180, 180, and 170 °C from the hopper to the die. After processing, the compositions obtained (Table 1) were immediately water-cooled and pelletized,

**Table 1** Compositions of PHAx 10007 and PHBV blends prepared *via* extrusion, expressed in mass (%) and in terms of copolymer composition of P(3HB-*co*-4HB) and PHBV (%) in the blends

Blend composition [%]		Copolymer composition[%]		
Identification	PHAx 10007	PHBV	P(3HB- <i>co</i> -4HB)	PHBV
PX	100	0	50	50
PHBV	0	100	—	100
PHBV_10PX	10	90	5	95
PHBV_20PX	20	80	10	90
PHBV_30PX	30	70	15	85
PHBV_40PX	40	60	20	80
PHBV_50PX	50	50	25	75



while only the pure PX needed to be pelletized 24 hours after being water-cooled due to slow crystallization.

After extrusion, the pellets were dried in a vacuum oven overnight at 70 °C. A 30 mm cylinder Engel E-Mac 50 injection molding machine was subsequently used for the injection molding process to produce samples for mechanical testing and shrinkage analyses. In the machine, the temperatures were 145 °C, 170 °C, 180 °C, and 175 °C in zone 4, the injection pressure was 600 bar, the dosage was 36 cm<sup>3</sup>, the injection speed was set at 16 cm<sup>3</sup> s<sup>-1</sup>, the holding pressure was set at 400 bar, the mold temperature was set at 55 °C, and the cooling time was 25 s.

Films were also produced to perform the biodegradation test. For this purpose, the blends were subjected to thermocompression *via* a Fontijne Presses machine, model LabEcon 600. The temperature and pressure were 185 °C and 37.5 kN, respectively.

Fourier transform infrared spectroscopy (FTIR) spectra of the polymer films were obtained in the range of 4000–500 cm<sup>-1</sup> on a Nicolet Summit Pro spectrometer (Thermo Fisher Scientific) *via* an ATR crystal accessory.

PHBV and the blends were subjected to thermal analysis *via* differential scanning calorimetry (DSC) on a TA Instruments Discovery DSC 25 instrument under a nitrogen atmosphere, with the temperature varying from –50 to 190 °C. The degree of crystallinity was determined *via* eqn (1) below:

$$X\% = \left( \left( \frac{\Delta H_m}{\text{PHBV}_w \times \Delta H_p} \right) \times 100 \right) \quad (1)$$

where  $\Delta H_m$  is the melting enthalpy of the system,  $\text{PHBV}_w$  is the polymer weight fraction in the sample, which only accounts for the presence of 4HB, and  $\Delta H_p$  is the melting enthalpy of the supposedly 100% crystalline polymer, for which the PHBV is at 146 J g<sup>-1</sup> (Carli, Crespo, and Mauler, 2011).<sup>50</sup> Thermogravimetric analysis was conducted *via* a TGA5500 instrument from TA Instruments under a N<sub>2</sub> atmosphere with a scanning range of 0–700 °C and a heating rate of 10 °C min<sup>-1</sup>.

X-ray diffraction (XRD) was evaluated *via* a Bruker X-ray diffractometer (model D6 Phaser). The incident radiation used was Cu-K $\alpha$  ( $\lambda = 1.5406 \text{ \AA}$ ). The sweep was selected between 5 and 45° (2 $\theta$ ) at a speed of 2° min<sup>-1</sup> and a power of 40 kV/30 mA. Through XRD, for comparison with the DSC values, the degree of crystallinity was calculated from the peak areas. The calculations were conducted *via* eqn (2):

$$X\% = \left( \frac{\sum A_p}{A_{\text{total}}} \right) \times 100 \quad (2)$$

where  $\sum A_p$  is the sum of all peak areas and  $A_{\text{total}}$  is the total area of the spectrum. This analysis was performed *via* Origin Pro software from OriginLab Corporation.

Tensile testing followed ISO 527 standards on a Zwick UPM 14740 ZMART. To evaluate the mechanical properties of the samples, a PRO Zwick BZ1-EXZW013 machine with an extensometer was used. The samples were tested through an axial force; the thickness and width were measured, and at least five measurements were carried out for each material. To analyze the impact resistance properties, 10 notched samples of each compound were subjected to Charpy impact tests on a Zwick PSW B5113.300 machine following ISO 179-1 standards.



The shrinkage of the 60 × 60 mm square injection-molded samples was analyzed. The measurements took place 1 h, 24 h, 7 days, and 21 days after the injection; the values were obtained in the flow direction and against the flow direction. Thus, the shrinkage values were calculated according to the dimensions *via* the following formula:

$$S = \frac{X_{mc} - X_{sp}}{X_{mc}} \quad (3)$$

where  $S$  is the shrinkage,  $X_{mc}$  is the dimension (length or width) of the mold cavity, and  $X_{sp}$  is the dimension of the sample. The measurements were taken *via* a Mitutoyo Absolute digital measuring clock with an accuracy of 0.02/±0.0010, in which 3 measurements were taken for each dimension. This methodology and graphic trend line were based on the methods of Kościuszko, Marciniak, and Sykutera (2020).<sup>20</sup>

The soil biodegradation test was based on the ISO 16929 standard, which is a crucial step in the ASTM D6400 evaluation process, in addition to other studies,<sup>21–23</sup> and carried out for 16 weeks. For the soil preparation, 90% of the garden soil was mixed with 10% active compost. The moisture of the soil mixture was adjusted and maintained at 80% or more of the maximum amount of water the soil could hold, and its weight was checked during the experiment. After that, the mixed soil and films that were being degraded were placed in aluminum boxes and sealed. Weight loss was used to measure biodegradation *via* eqn (4).

$$\text{Weight loss (\%)} = \frac{M_1 - M_2}{M_1} \times 100 \quad (4)$$

where  $M_1$  is the initial weight obtained before biodegradation and  $M_2$  is the final mass obtained after biodegradation. The samples were washed with water to remove any soil residue, dried for 24 hours to remove excess moisture, and weighed again to assess weight loss due to biodegradation. Photos were taken of the degraded films using an iPhone 11 smartphone camera.

For the 3D-printing analyses, all the compositions used to produce monofilaments were processed *via* an extruder 3Devo Composer 450 filament maker. The temperatures for PHBV and the blends were 165 °C, 180 °C, 180 °C, and 175 °C in the 4 temperature zones; the PX needed temperature reductions of 165 °C, 170 °C, 170 °C, and 175 °C; the screw speed was 4 rpm; the puller and winder were automatically adjusted; and the fan speed was 100%.

For all the 3D-printing analyses, a 3D printer, Mass Portal Pharaoh ED 30, was used with a 0.40 mm output extruder nozzle. The slicing program used to convert 3D models into instructions that a 3D printer can understand was simplified to 3D, and other parameters used for printing are described in Table 2.

The first test of printability was performed according to the literature,<sup>24</sup> where calibration towers were produced at different temperatures in specific zones. It was possible to evaluate parameters such as string, bridging, and adhesion on the bed. The model used for this test, which was downloaded from the site <https://www.thingiverse.com> and was accessed in March 2023,<sup>25</sup> is shown in Fig. 1. Based on DSC analysis and the literature,<sup>26</sup> the temperatures were set from highest to lowest. The tower was composed of eleven zones, set from 225 °C to 175 °C with steps of 5 °C.

Table 2 Parameters configured for 3D printing *via* simplified 3D software

Filament diameter (mm)	1.75
Nozzle (mm)	0.4
Layer thickness (mm)	0.2
Printing speed (mm s <sup>-1</sup> )	50
Printing temperature (°C)	225–175
Bed temperature (°C)	80
Fan speed (mm s <sup>-1</sup> )	100
Brim (layers)	15
Infill (%)	20
Adhesion spray	Yes

To quantify the warping effect on the printed parts, a coefficient was determined based on the literature.<sup>27</sup> A part with a theoretical height of 3 mm was used to carry out the test. The coefficient was calculated according to eqn (5) using the ratio of the theoretical sample size to the actual printed size.

$$\text{Warping coefficient} = \frac{\text{total theoretical height of the sample (3 mm)}}{\text{maximum height reached by the sample}} \quad (5)$$

After printing started, the process was visually monitored until the part was detached from the printing table. The value of the maximum real height up to that point was then noted for the calculations. The printing temperature was set at 190 °C, and the printing platform was used without adhesive spray.



Fig. 1 Design photo of the calibration tower.



A statistical analysis was performed on the results of the tensile and impact tests. The significance of the differences between the groups, given as  $p < 0.05$ , was calculated *via* analysis of variance (ANOVA), followed by the Tukey test *via* OriginLab 2023b software.

## Results and discussion

The blends consisting of PHBV and PX were successfully produced by extrusion, and all the compositions were analyzed *via* FTIR. Fig. 2 shows the FTIR spectra for all the compositions produced. The pure PHBV shows bands at 2978 and 2923  $\text{cm}^{-1}$  attributed to the stretching vibrations of the C–H group.<sup>28</sup> The bands at 1740  $\text{cm}^{-1}$  and 1718  $\text{cm}^{-1}$  represent the deformation of the ester group (C=O) in the two regions, respectively, with one representing the amorphous region and the other the crystalline region.<sup>29</sup> The bands at 1452 and 1379  $\text{cm}^{-1}$  indicate the stretching vibrations of the –CH groups.<sup>30</sup> The bands 1261, 1225, and 1181  $\text{cm}^{-1}$  refer to the symmetrical and asymmetrical stretching of the C–O–C group.<sup>31</sup>

The FTIR spectrum of PX shows that most of the peaks are very similar to those of PHBV, indicating that they have comparable structures and bonding, with only the intensities of the absorbance bands varying. This intensity variation is characteristic of P(3HB-*co*-4HB).<sup>32</sup> The intensities of the peaks increased proportionally with the addition of PX to the PHBV. Similar results were reported by Ong, Chen, and Don (2023)<sup>33</sup> for a blend of polylactic acid (PLA) and P(3HB-*co*-4HB), in which FTIR spectroscopy indicated an increase in the intensity and appearance of P(3HB-*co*-4HB) bands proportional to their addition and a decrease in the intensity of the PLA peak.

Wang *et al.* (2010)<sup>35</sup> developed blends of PHBV and P(3HB-*co*-4HB), in which Fourier transform infrared spectroscopy (FTIR) analysis revealed that increasing the content of P(3HB-*co*-4HB) increased the interactions with PHBV. However, the

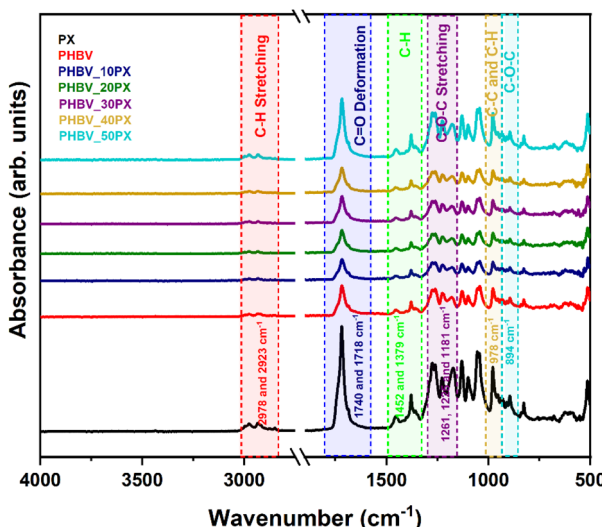


Fig. 2 FTIR spectra of the blends prepared by extrusion: PX, PHBV, PHBV\_10PX, PHBV\_20PX, PHBV\_30PX, PHBV\_40PX, and PHBV\_50PX.



findings of the present study contrast with this observation, as a reduction in the intensity of the bands was observed with the addition of P(3HB-*co*-4HB). The authors also reported that PHBV plays a crucial role in the helical molecular configuration and crystallization of the P(3HB-*co*-4HB) network, where two “left-handed” helical molecules are aligned with their ester groups in an antiparallel orientation. As the content of P(3HB-*co*-4HB) increases, the separation of the two helices in the antiparallel direction occurs, which limits their deformation.<sup>34,35</sup> The spectrum presented in Fig. 2 shows no significant shift in the bands or the formation of new bands. This observation may suggest immiscibility of the blend, potentially due to the absence of chemical interactions following melt blending, as indicated in the literature. Alternatively, this lack of change could also be attributed to the structural similarity between the PX and PHBV components. Consequently, the FTIR analysis alone does not provide a definitive conclusion regarding the miscibility of these biopolymers.<sup>36,37</sup>

The thermogravimetric analysis (TGA) and differential thermogravimetric analysis (DTG) results for the pure polymers and all the produced components are displayed in Fig. 3 and Table 3, respectively. The degradation temperature of pure PHBV was in the range of 218 °C for  $T_{5\%}$  and 257 °C for  $T_{Endset}$ , which is lower than that reported in the literature.<sup>38–40</sup> Rodriguez-Uribe *et al.* (2021)<sup>41</sup> reported that the initial degradation temperature of PHBV is 238 °C; however, rapid degradation with weight loss is characteristic of PHBV. The thermal degradation process of PHBV is directly linked to the random chain scission of ester groups, resulting in the decomposition of the six-membered ester ring, thus eliminating  $\beta$ -hydrogen to generate olefins and altered oligomers.<sup>42</sup>

The PX has an onset temperature of 233 °C and an endset temperature of 305 °C. This temperature range is in agreement with works in the literature, such as that of Omura *et al.* (2021),<sup>43</sup> who evaluated the thermal degradation of P(3HB-*co*-16 mol%-4HB) under various heating ramps, in which decomposition occurred only in a single stage. Han *et al.* (2012)<sup>44</sup> created composites with a matrix of P(3HB-*co*-4HB) and silica and discovered that the polymer undergoes thermal decomposition during processing, making melting difficult and emphasizing the importance of using materials that improve thermal stability.

Blending of PHBV and PX increased the thermal stability of the blends, following the PX trend. However, the increase did not show linear behavior, so the degradation temperatures varied among all blend percentages, emphasizing PHBV\_50PX, which reached the highest temperature. However, given the blends’ degradation temperature ranges, these variations are considered insignificant.

This behavior of increased thermal stability was also identified by Kovalcik *et al.* (2021),<sup>45</sup> who developed blends of P(3HB-*co*-4HB) and PLA, in which they reported that the blend between the two polymers was the most stable material among the other compositions evaluated using only plasticizers. Feijoo *et al.* (2022)<sup>46</sup> developed PHBV/PHBH blends by evaluating general properties, particularly their thermal properties. The medium-chain-length-PHA side chains, which sterically block the distribution of the six-membered transition structure, are responsible for the observed improvement in thermal stability when the PHBH content is increased.

The thermal transitions of the blends were evaluated *via* DSC. Fig. 4 shows the cooling (a) and second heating (b) curves of pure PHBV and PX and their blends. The first and second heating and cooling values and their respective enthalpies



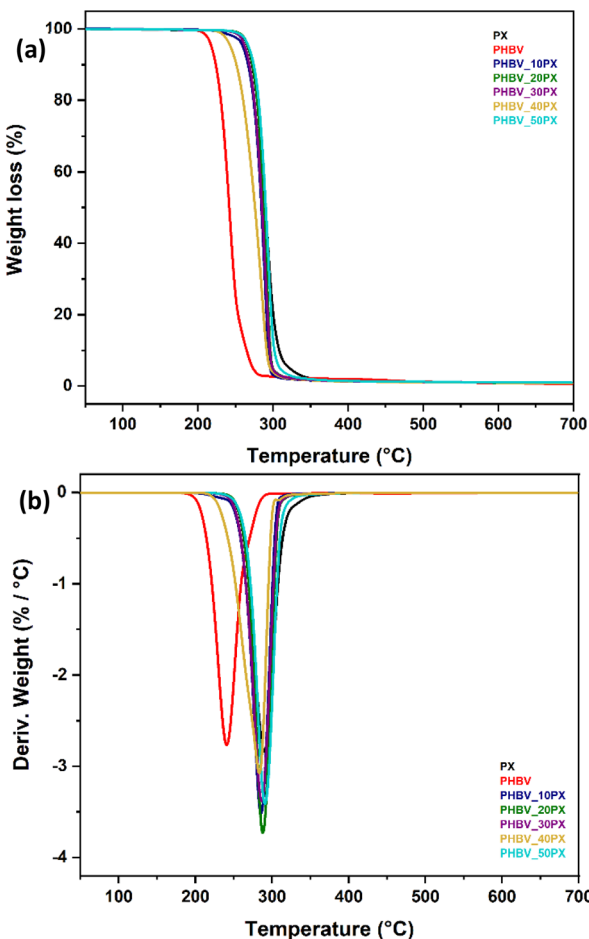


Fig. 3 Thermogravimetric analysis (a) of PHBV, PX, and their blends in different compositions, and the derivative thermogravimetry (b).

are given in Table 4. For all blends, the DSC curves show the formation of two melting peaks on the first heating curve. The observed behavior is explained by secondary crystallization, which occurs when a polymer recrystallizes after

Table 3 The thermal decomposition characteristics of PHBV, PX, and their blends with varying PX contents

Compositions	Onset (°C)	Peak (°C)	Endset (°C)	$T_{5\%}$	$T_{25\%}$	$T_{50\%}$	$T_{75\%}$
PHBV	198.3	240.7	256.5	218.0	233.5	242.6	250.3
PHBV_10PX	218.4	285.5	295.5	259.5	276.4	284.4	290.1
PHBV_20PX	230.9	287.8	297.4	266.9	280.8	287.6	292.6
PHBV_30PX	230.1	286.3	297.1	262.6	277.2	285.2	291.4
PHBV_40PX	220.5	280.8	294.1	243.5	263.4	275.9	285.5
PHBV_50PX	234.5	290.7	301.6	267.6	282.8	290.3	296.2
PX	232.9	289.7	304.8	266.5	281.1	289.8	298.0

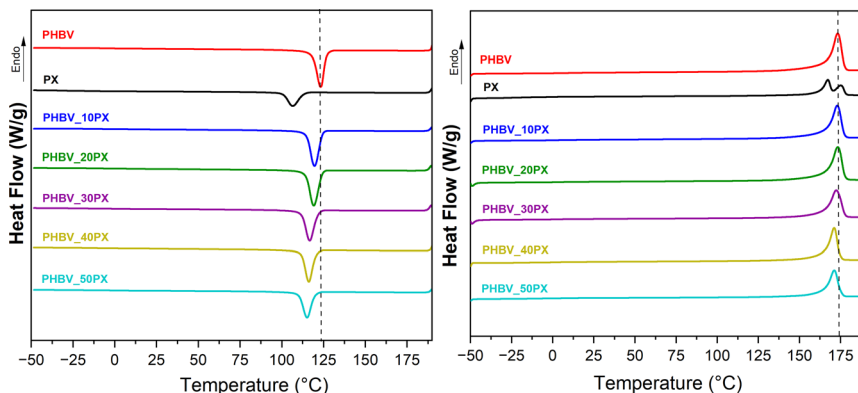


Fig. 4 Differential scanning calorimetry (DSC) curves for pure PHBV and PX and their blends: (a) cooling step and (b) the 2nd heating step.

processing. In this scenario, the polymer chains tend to relax into a lower-energy state, allowing for increased crystallization.<sup>47</sup>

The crystallization rate is measured using cooling crystallization curves. The blends presented a slight reduction in the crystallization temperature for the compositions with PX inserted. This behavior is expected due to the presence of PX, which has a lower crystallization temperature than PHBV. This difference arises from its amorphous phase and the increasing 4HB content in the composition, which reduces the spherulitic growth rate. The increased stereo-hindrance effect of the side groups delays solidification slightly.<sup>18</sup>

Furthermore, DSC revealed that the crystallization and crystal melting temperatures slightly increased for the 10 and 20% compositions. These findings might be related to the lower degree of crystallinity of PX. The literature reports that HB units act as defects, altering the packing of the 3HB network more than HV units do.<sup>48</sup>

During the second heating stage, as the amount of PX in the blend increases, the melting points remain relatively unchanged, and the blends lack the second melting peak observed in pure PX. This can be attributed to the dominance of the

Table 4 Thermal transition temperatures with their respective enthalpy energies for PHBV, PX, and their blends, as determined via DSC

Sample	1° heating		Cooling		2° heating		
	$T_m$ [°C]	$\Delta H_m$ [J g <sup>-1</sup> ]	$T_c$ [°C]	$\Delta H_c$ [J g <sup>-1</sup> ]	X%	$T_m$ [°C]	$\Delta H_m$ [J g <sup>-1</sup> ]
PHBV	170.5	87	123.6	-87	66.2	173.1	97
PHBV_10PX	171.3/177.6	77	119.9	-78	61.5	173.8	90
PHBV_20PX	171.0/176.8	82	119.5	-78	62.5	173.3	91
PHBV_30PX	169.2/175.6	73	117.3	-73	63.1	172.0	80
PHBV_40PX	167.8/175.2	71	116.1	-69	61.3	171.0	79
PHBV_50PX	167.2/175.6	65	115.3	-60	64.0	170.6	73
PX	166.6/174.5	50	106.9	-41	50.2	167.4/175.7	55

crystalline phase of PHBV. The high 4HB content in PX highlights the incompatibility in forming two-phase crystals, resulting in broadened melting peaks and additional transitions at higher temperatures.<sup>49</sup> The absence of distinct double melting peaks in the blends suggests strong interactions between the two copolymers, likely due to their similar molecular structures. Both PHBV and PX have a low HV content of approximately 2–3%, making 3HB the primary contributor to the crystallization response. The observation of a single crystallization peak indicates effective blending and higher crystallinity, as only one unified crystallization phase is present.<sup>47</sup>

XRD, shown in Fig. 5, was used to identify the crystallographic planes in the pure polymers and blends at various percentages, and similar diffraction peaks were visible in each sample. The diffractograms show diffraction peaks characteristic of PHBV at approximately  $2\theta = 13.4^\circ$ ,  $16.8^\circ$ , and  $20.1^\circ$ , corresponding to the (020), (110), and (100) crystallographic planes of the orthorhombic structure of the PHB unit cell, respectively, and peaks at  $20.1^\circ$ ,  $21.5^\circ$ ,  $22.6^\circ$ ,  $26.7^\circ$ , and  $27.1^\circ$ , corresponding to the (101), (111), (121), (130), and (040) planes, respectively.<sup>26,50,51</sup>

An increase in the percentage of PX polymer in the blends did not result in changes in the main peaks reported for the PHBV phase; however, the intensity of the peak at  $26.7^\circ$  was suppressed in the blends. The lack of a shift in the peaks compared with those of the pure polymers suggested that adding PX to the PHBV matrix did not significantly change the crystallization kinetics, since both polymers have P3HB as the domain, which results in crystal formation; thus, when mixing these polymers it seems that the lattice crystal structure remains unchanged.<sup>52</sup>

PHB, PHV, and P4HB homopolymers share a similar orthorhombic crystalline structure, differing only in their lattice parameters. For copolymers, PHBV crystallizes in either the PHB or PHV lattice, depending on the 3HV content, with the transition occurring below 37 mol%. A similar trend is observed in P(3HB-*co*-4HB), where the shift to the 4HB lattice takes place at approximately 50 mol% of the 4HB comonomer.<sup>18</sup>

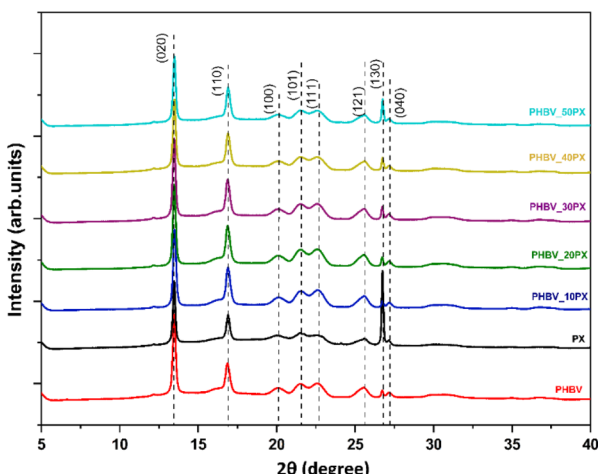


Fig. 5 XRD patterns for PHBV and PX and their blends with different contents of PX.



Table 5 Degrees of crystallinity ( $X_c$ %) of all blends, PHBV, and PX polymers

PHBV	63.6
PX	64.6
PHBV_10PX	68.8
PHBV_20PX	67.2
PHBV_30PX	65.5
PHBV_40PX	66.8
PHBV_50PX	67.8

Table 5 presents the degrees of crystallinity  $X_c$  (%) for all the blend compositions calculated from the XRD peak areas. Incorporating PX into the blend did not result in significant changes in the degree of crystallization. Moreover, the obtained crystallization degree values are consistent with the results observed in the DSC analysis. This consistency indicates that the thermal properties of the PHBV\_50PX blend closely resemble those of pure PHBV.

The results from the X-ray diffraction (XRD) analysis were consistent with the differential scanning calorimetry (DSC) results, regarding the degree of crystallinity for all compositions tested. The crystallinity values obtained from both DSC and XRD indicate that mixing PHBV and PX did not alter the crystallization mechanism. This is because both polymers share a similar structural composition, with a domain from 3HB, which influences their crystallinity behavior.<sup>35</sup> Concerning the most important thermal properties, the DSC analysis reveals a decrease in melting enthalpy with an increase in PX content, as well as the reduction of the crystallization temperature, as detailed in Table 5. Additionally, the XRD patterns in Fig. 5 show variations in peak intensity, particularly at 26.7°. These findings indicate an increase in the amorphous phase within the blend with higher PX concentrations, primarily due to the contribution of 4HB.<sup>46,53</sup> Thus the overall crystallinity of the blends was reduced with the inclusion of the P(3HB-*co*-4HB) copolymer present in PX.

To assess the mechanical behavior of the blends, Fig. 6 shows the results from the tensile and impact tests; the corresponding values with the statistical analyses are detailed in the ESI (Table S1†). The pure PHBV exhibited a tensile strength of 42.9 MPa and an elongation at break of 1.2%, which is consistent with findings from previous studies<sup>52,54,55</sup> These results indicate that PHBV demonstrates low-strain behavior, which is characteristic of brittle fracture.<sup>56</sup> This brittleness is attributed to the crystalline structure of PHBV.<sup>57,58</sup> The impact resistance value of pure PHBV, which was the lowest among the samples tested, further corroborates this behavior. Although the statistical analysis did not reveal significant differences in impact resistance among the compositions containing 10%, 20%, and 30% PX, the trend suggests that blending improves the impact resistance compared with that of pure PHBV.

On the other hand, PX displayed a distinct behavior, characterized by higher impact energy and greater deformation, indicating its increased ductility.<sup>59</sup> This behavior is attributed to the presence of the 4HB monomer, which enhances the amorphous region and increases chain flexibility. Additionally, research indicates that the reduction in spherulite size and the lower crystallization rate within the 4HB segment contribute to improved elongation and a reduction in the interfacial impact area within the 3HB fraction.<sup>60</sup>



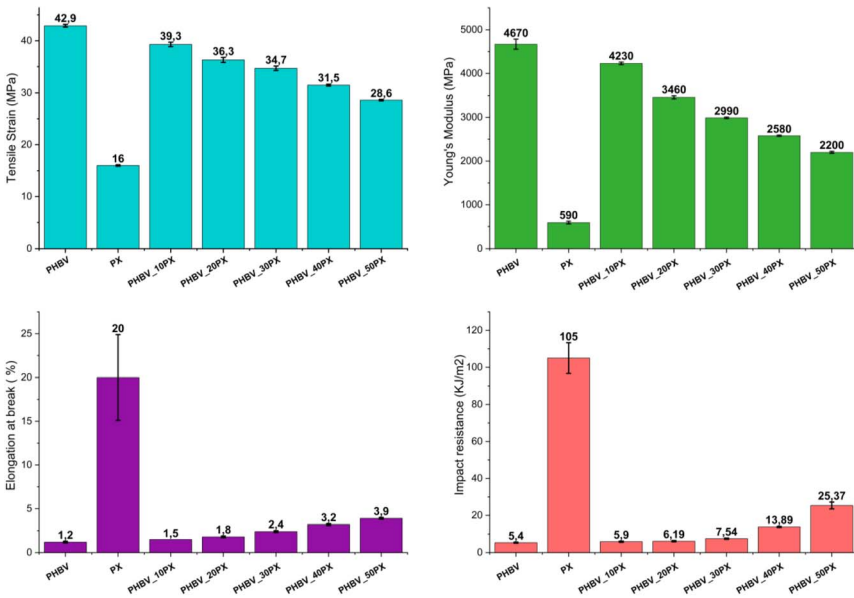


Fig. 6 Mechanical performance of all blend compositions: tensile strain, Young's modulus, elongation at break, and impact resistance.

As the proportion of PX increased, the mechanical properties of the blends exhibited notable variations. Compared with pure PHBV, the tensile strength and Young's modulus for PHBV\_10PX decreased by 8.4% and 9.4%, respectively. For PHBV\_50PX, these reductions were more pronounced, with the tensile strength and Young's modulus decreasing by 33.3% and 53%, respectively. In opposition, there was an increase in elongation and impact resistance, with the PHBV\_50PX blend achieving the highest values among the blends. Both blends exhibited complete breakage during the impact test, indicating that the fundamental brittleness of the material was not entirely mitigated.

The elongation increased from 1.2% for pure PHBV to 3.9% for PHBV\_50PX. However, this difference was not statistically significant, indicating that incorporating PX into PHBV did not enhance flexibility to the extent anticipated. This suggests that the reduction in tensile strength was the primary factor contributing to the observed decrease in Young's modulus. The tensile test results may be attributed to the incompatibility between P(3HB-*co*-4HB) and PHBV during the mixing process. This immiscibility, which was suggested by earlier FTIR analysis, could have led to phase separation, thereby affecting the mechanical properties of the blend.<sup>61</sup>

When observing impact resistance, a significant increase was noted with 40 and 50% PX. This finding indicates that PX works better at absorbing energy rather than providing elongation in the blend. This could be due to the immiscibility of P(3HB-*co*-4HB) in the PHBV matrix, making the amorphous copolymer act as a rubber filler with increasing elongation and energy of impact. However, the values reached by PHBV\_50PX are similar to those of commercial polymers such as PLA,<sup>62</sup> PP,<sup>63</sup> LDPE,<sup>64</sup> HDPE,<sup>65</sup> and PET.<sup>66</sup>

Lijing Han *et al.* (2012)<sup>67</sup> blended PLA with P(3HB-*co*-4HB) and reported that adding P(3HB-*co*-4HB) resulted in an increase in elongation and a decrease in tensile strength and modulus, findings that align with the observations in our research.

Fig. 7 presents the shrinkage of square samples produced by injection molding for all compositions, measured in the direction of the injection flow and against the direction of flow. Owing to its crystalline nature, PHBV presented the highest shrinkage values regardless of the flow direction. Specifically, in the direction of the injection flow, PHBV shrank by 1.53% 1 h after injection, corresponding to the primary crystallization phase. This value increased to 1.68% after 24 hours. The secondary crystallization process, which was analyzed over 21 days, resulted in a final shrinkage of 1.84%.

The shrinkage values measured against the flow direction were slightly lower, with values of 1.42% in 1 hour, 1.62% after 1 day, and 1.82% after 21 days. These results suggest that PHBV exhibited uniform contraction and effective material distribution throughout the mold.<sup>68</sup> The similarity in values can be explained by the isomeric nature of the PHBV. This indicates that the atoms are arranged similarly in each repeat unit, resulting in a consistent crystalline structure throughout the chain.<sup>69</sup>

For pure PX, the shrinkage rates were 1.13% and 1.20%, respectively, considering the difference in the injection flow direction, between one hour and 1 day after injection. After 21 days, the shrinkage reached 1.28%. Similar values were discovered against the injection flow direction, suggesting that PX has a constant distribution behavior for the injection molding samples. Therefore, the presence of P(3HB-*co*-4HB) in the composition of PX, which provides the amorphous structure with the 4HB monomer, helps explain shrinkage equivalence values as a result of its random formation.<sup>70</sup>

For the blends, shrinkage consistently decreased as the PX content increased. This trend can be primarily observed in the graph for in the flow direction, where shrinkage progressively decreases with increasing PX in the blend.

Shrinkage is a significant factor for injected molded products, and the results obtained here show that the introduction of PX in PHBV has a large effect on shrink reduction. The main reason is the inclusion of a more amorphous phase in

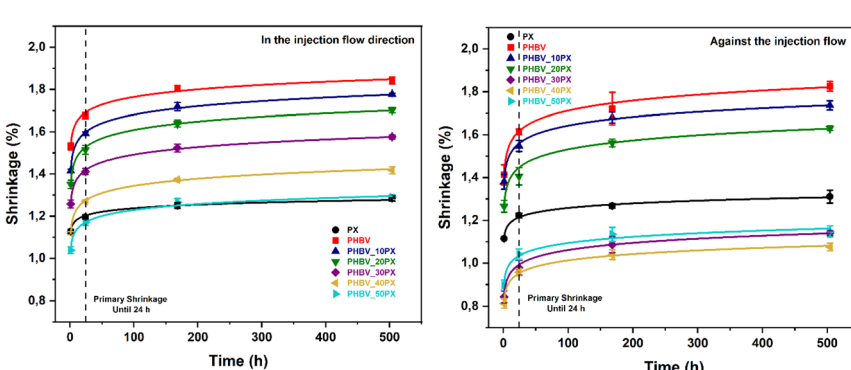


Fig. 7 Shrinkage of the samples of all compositions: (left) in the direction of the injection flow; (right) against direction of the injection flow, with 400 bar of holding pressure.



the blend. When a polymeric material contains more crystalline phases, the relaxation time is greater, resulting in increased internal stress and consequently greater shrinkage.<sup>71</sup> Additionally, the literature shows that semicrystalline polymers have a more compact molecular arrangement and lower free volume, which can also reduce shrinkage.<sup>72</sup>

The graph against the flow direction shows another type of behavior, in which the compositions with more than 20% PX had lower shrinkage values than those with pure PX. The composition with PHBV\_40PX had the lowest shrinkage values, with 0.81%, 0.95%, 1.04%, and 1.08% representing 1 hour, 1 day, 7 days, and 21 days, respectively.

The observed variation in shrinkage may be attributed to anisotropy effects, which arise from the alignment of the polymer chains in the direction of the injection flow. This alignment results in lower and more unpredictable shrinkage values because of the restricted mobility of the chains against the flow direction.<sup>73</sup>

The results for soil degradation over time in weeks are depicted in Fig. 8; the detailed values are presented in the ESI (Table S2†). For pure PHBV, initial degradation was minimal during the first week, likely due to the time required for the establishment of an environment conducive to enzyme activity and microbial colony formation. Following this period, a continuous increase in degradation was observed, culminating in a mass loss of 95% at 14 weeks and nearly complete degradation of the film at 16 weeks, with a mass loss of 97%.

These findings are consistent with those of previous studies, such as that by Iggui *et al.* (2015),<sup>74</sup> who reported mass losses of 19% and 70% after 21 and 70 days, respectively, for pure PHBV, compared with the values of 24% and 63% observed in this study after 4 and 10 weeks. Additionally, Salomez *et al.* (2019),<sup>75</sup> in their analysis of the biodegradation curves of PBSA and PHBV over 60 days, reported that PHBV was completely degraded, further supporting the results observed here.

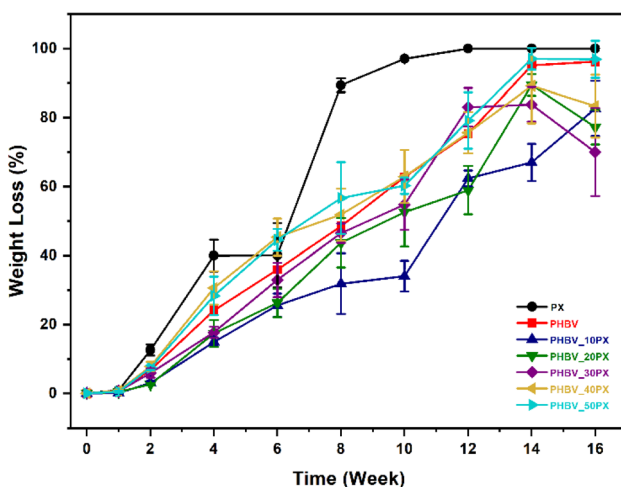


Fig. 8 Weight loss of all the samples over time was determined by the soil degradation process.



Other authors<sup>76–78</sup> have reported different values, as well as different methods. According to Chan *et al.* (2021),<sup>79</sup> the thickness of the films can impact the various surface areas and densities of the polymer, which can affect the mass loss values.

Table 6 presents the film thickness values, revealing significant variations across the different compositions. These variations suggest that thickness may have a considerable influence on the degradation process of the samples. The relatively rapid degradation of pure PHBV observed in this study further substantiates this hypothesis, indicating that film thickness plays a critical role in degradation dynamics.

It is important to consider how the processing method, particularly 3D printing, may influence the biodegradation behaviour of the material. Increased surface roughness and exposed ridges from the layer-by-layer deposition process used in 3D printing may promote microbial attachment and enzymatic breakdown. Biodegradation might be accelerated by this larger surface area in comparison to samples that are conventionally molded or flat films.<sup>80,81</sup> Even though printed and non-printed specimens were not directly compared in this study, future research should examine how internal microstructure variations and surface morphology affect the blends' rate of degradation.

The polymer hydrolysis process is initiated by the exogenous enzymes of microorganisms when a biofilm develops on the surface of a polymeric film. PHBV breaks down in this way from the surface to the center of the film because the enzymes that hydrolyze the ester groups are unable to pierce deeply into the polymer due to its high crystallinity and hygroscopicity. Because the polymer chains are compacted in the crystalline regions, water penetration is difficult, making humidity an important factor in controlling microbial growth and supporting the hydrolytic environment.<sup>74,82</sup>

For PX, a rapid trend in the biodegradation rate was observed, where it exhibited the greatest mass loss among all the compositions. By the end of the 12 week evaluation period, the films had completely degraded. This behavior aligns with certain values reported in the literature, especially when considering the percentage of P(3HB-*co*-4HB) present in the PX blend.

Wen & Lu (2012)<sup>83</sup> evaluated a P(3HB-*co*-4HB) polymer matrix with varying 4HB contents and reported that all compositions exhibited a mass loss exceeding 5% after 60 days in soil. Notably, the study revealed an increase in mass loss, indicative of greater degradation, as the 4HB content in the composition increased, with the 15% 4HB composition resulting in the highest degradation rate. The authors attributed this trend to the percentage of crystallinity in the matrix, which

**Table 6** Film thicknesses of PHBV, PX, and their blends produced by thermocompression

PHBV	0.0823 mm $\pm$ 0.0101 d
PX	0.1408 mm $\pm$ 0.0105 a
PHBV_10PX	0.1069 mm $\pm$ 0.0118 c
PHBV_20PX	0.1108 mm $\pm$ 0.0102 c
PHBV_30PX	0.1136 mm $\pm$ 0.0109 b,c
PHBV_40PX	0.1197 mm $\pm$ 0.0109 b
PHBV_50PX	0.1200 mm $\pm$ 0.0128 b

a, b, c, d: different letters indicate a group with a significant difference ( $p > 0.05$ ) between the means according to Tukey's test.



is influenced by the 4HB content and affects the proportion of the amorphous phase within the structure. This finding was also confirmed by Volova *et al.* (2017),<sup>84</sup> who evaluated the behavior of PHAs with different chemical compositions and reported that P(3HB/4HB) had the highest degradation rate in soil.

For the compositions consisting of a mixture of both copolymers, a reduction in the degradation rate was observed up to 30% PX content. The composition with 10% PX presented the lowest degradation rate, achieving 82.64% mass loss at 16 weeks, whereas the 30% PX composition presented the lowest overall degradation rate, with a mass loss of 70% after the 16 week period. As the PX content increased beyond 30%, the degradation behavior began to resemble that of pure PX, with the degradation curves for the 40% and 50% PX compositions closely aligning with those observed for pure PHBV. This variation is directly linked to the structures formed by the blend, and the balance between the components, as identified in the previous characterization, directly influences the properties. Wang *et al.* (2010)<sup>35</sup> reported that when the P3HB/4HB content increases without changing the crystalline structure of PHBV, the crystallinity of the PHBV and P3HB/4HB blend for spherulites decreases.

Fig. 9 shows macroscale photographs of the films over the degradation time. Notably, the surface of the PHBV has a smooth appearance, which is characteristic of this type of polymeric film.<sup>85,86</sup>

A similar appearance is found in the pure PX film and the other compositions because of the amount of PHBV present in the composition. For all the compositions, an effect of fading color of the films over the degradation time in weeks was noted. This fact is common, as indicated by Zaidi *et al.* (2019),<sup>87</sup> who strengthened PHBV with unidirectional flax and tempered it with PBAT or ENR50 and found the same fading aspect, which they attributed to the “micropitting” effect, *i.e.* microscopic cavities on the film’s surface produced by chemical degradation caused by the attack of microorganisms.

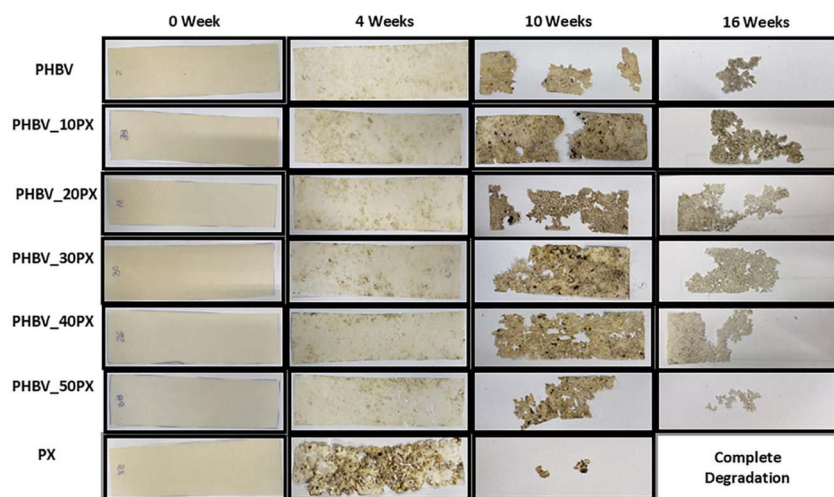


Fig. 9 Photography of the PHBV and PX films and their blends during soil degradation.



For pure PHBV, there were no significant changes in the surface of the film for up to 2 weeks, which can be related to the low weight loss; at 4 weeks, it was possible to observe the first points of attack by microorganisms and the appearance of holes after 6 weeks of testing. However, for pure PX, owing to the higher percentage of P(3HB-*co*-4HB), the degradation process began after only 2 weeks of testing, and at 4 weeks, it was possible to observe cavities in the films and severe signs of degradation.

Other studies on PHBV yielded similar results. They reported that physical signs of deterioration in the samples caused by microbial attack included loss of gloss, decreased thickness and area, and the presence of holes and tears. Additionally, PHA undergoes a hydrolysis reaction, during which the ester bonds in the linear chains break, resulting in mass loss and a decrease in molecular weight.<sup>88</sup> Therefore, the mass loss data and visual observations indicate a surface erosion mechanism, with progressive surface roughening and the film samples becoming thinner.

These results reinforce the hypothesis that incorporating P(3HB-*co*-4HB) can effectively modulate the biodegradation rate of PHBV, making these blends promising candidates for applications where efficient degradation is desirable. These findings not only underscore the potential of these blends for environmental applications but also highlight the need for further research into the effects of varying environmental conditions and the analysis of degradation byproducts to ensure safe environmental impact.

Fig. 10 presents the IR spectra of the films after 8 weeks of degradation. The spectra revealed that all the samples presented similar peaks after degradation, which was consistent with the microbial activity that led to the degradation of the materials.

This is evidenced by the appearance of peaks at  $3290\text{ cm}^{-1}$ , corresponding to N-H stretching,  $1542\text{ cm}^{-1}$  for N-H bending, and  $1083\text{ cm}^{-1}$  for P=O stretching, all of which are associated with the secondary amides of cellular proteins that are associated with nucleic acids.<sup>85</sup> The spectra indicate that the greater amount of

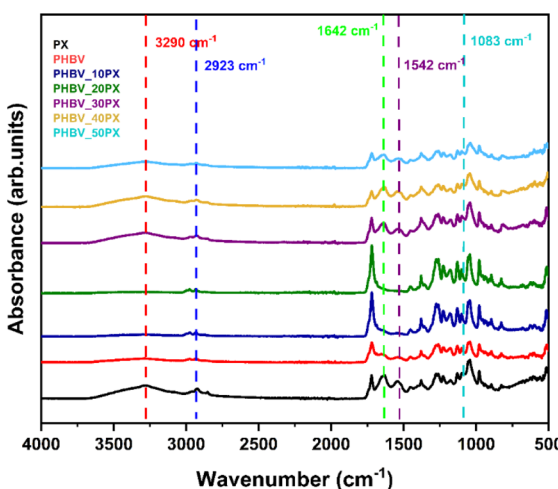


Fig. 10 FTIR spectra of the degraded blend films after 8 weeks of biodegradation.



the amorphous phase in the blends promoted the growth and penetration of the enzymes produced by the microorganisms responsible for film degradation. This is supported by the observation that these peaks were less pronounced in pure PHBV, as well as in the 10% and 20% PX compositions, with the peak intensity increasing in correlation with a higher PX content.

Furthermore, another indicator of film degradation is the reduction in the intensity of the peak at  $1923\text{ cm}^{-1}$ , which is associated with the breaking of  $=\text{CH}$  bonds as a result of the exo-cleavage activity of PHA depolymerase. The band at  $1642\text{ cm}^{-1}$ , corresponding to the  $-\text{C}=\text{C}-$  stretching vibration, is related to the cleavage of ester bonds.<sup>85,89</sup> Importantly, the structure of the remaining PHBV remained largely unchanged, suggesting that the degradation process progressed from the exterior to the interior of the polymeric films over time. Studies suggest that the absence of degradation byproducts, such as oligomers, which can be lost through leaching into the soil or washed away during the removal process, further supports the conclusion that degradation occurs gradually, moving inward from the film surface.<sup>85,86</sup>

3D-printing analyses were conducted on the blends, using filaments produced from the respective compounds. Fig. 11 shows three examples of the printed structures: one for each of the pure polymers, PHBV and PX, and one representing an intermediate composition of the PHBV\_30PX blend.

The quality of the geometric elements, such as the string on the bridge connecting the points on each floor, as well as elements such as subextrusion, porosity, and inclination, were considered in each temperature range applied to the floors.<sup>83</sup> The temperature range to be used in printing for these compounds was set between  $180\text{ }^\circ\text{C}$  and  $200\text{ }^\circ\text{C}$ .

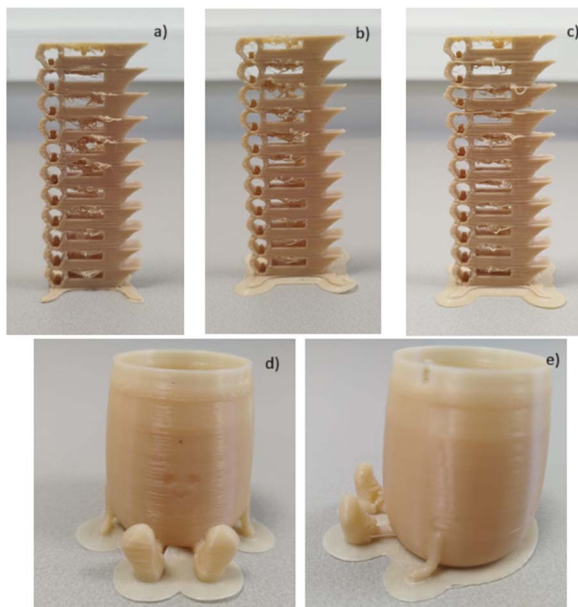


**Fig. 11** Photographs of 3D-printed calibration towers for PHBV (a), PHBV\_30PX (b), and PX (c); (d) and (e) are 3D-printed sample designs made from the blend PHBV\_30PX.



Following the successful production of the towers, additional objects with various geometries were printed under the selected conditions (Fig. 11). Visual examination of these printed objects confirmed that the material exhibited satisfactory printability, with no significant issues encountered during the printing process.

The warping coefficient is a dimensionless and practical measure, with lower values indicating a delayed manifestation of warping effects; a value of zero signifies the absence of observable warping.<sup>90,91</sup> The warping coefficient was determined for each sample by printing 20 mm × 20 mm × 3 mm cubes at the selected temperature. Based on the evaluation of the printing tower and the melt flow index (MFI), a temperature of 190 °C was chosen for the printing process. Fig. 12 presents a graph illustrating the warping coefficients across different compositions.

The PHBV material exhibits a strong warping coefficient due to its high and rapid crystallization. This directly impacts the adhesion time of the material on the printing platform. As the PX content in the blend increases, the warping coefficient noticeably decreases. These results may be associated with shrinkage in the injection-molded samples, which followed a similar decreasing trend. This suggests that with different processing methods, the defects in the PHBV of the blends tend to decrease.

Despite the decreased warping values of the blends, our tests unequivocally demonstrated that printing could not be accomplished without spray adhesive. This necessity occurred because of the difficulty of ensuring adhesion, for the first layer to stick to the table. The adhesion of the initial printing layer is indispensable to the printing process; insufficient adhesion results in the material peeling off the build platform.<sup>92</sup>

Fig. 13 presents images of the parts printed for warping coefficient measurement, where a visual reduction in the angle formed between the printed products and the surface is evident. This reduction is associated with decreased warping. Additionally, an improvement in the overall quality of the printed products can also be observed.

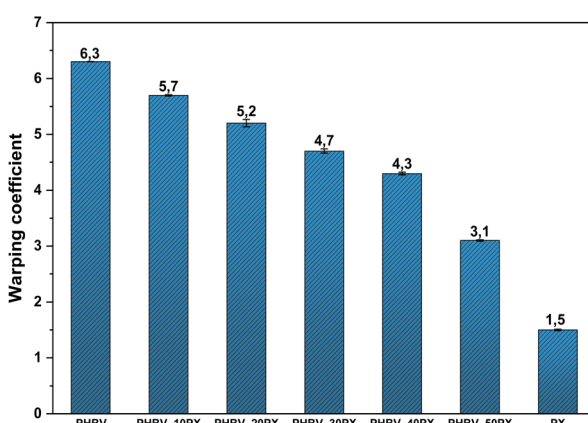


Fig. 12 Warping coefficients of all the pure polymers and blends.



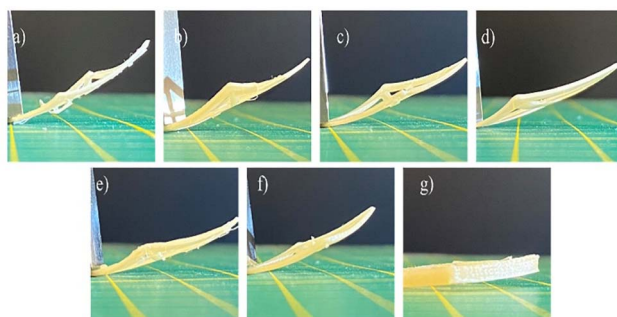


Fig. 13 Photos of the printed parts used to measure the warping coefficient. (a) PHBV, (b) PHBV\_10PX, (c) PHBV\_20PX, (d) PHBV\_30PX, (e) PHBV\_40PX, (f) PHBV\_50PX and (g) PX.

These findings indicate that warping is affected by the crystallinity of the blend. The samples with a relatively high PX content tended to warp less, which can be attributed to the increase in the amorphous phase, which resulted in reduced volume shrinkage when the samples were placed on a cooler build plate.<sup>93</sup> For 3D printing, the use of amorphous thermoplastic polymers is highly recommended because the lack of crystallization prevents shrinkage, in addition to their low temperatures allowing a reduction in internal stresses during cooling.<sup>94</sup> In this technique, material characteristics are crucial due to the high anisotropy of the process, where cooling heavily influences contraction during the deposition of threads in terms of temperature distribution.<sup>26</sup>

For the materials examined in this study, the factors contributing to poor adhesion, which in turn leads to the warping process, are primarily the high and rapid rate of crystallinity, which is predominantly induced by the PHBV, as evidenced by the XRD results. Additionally, the high polarity of PHBV may also play a significant role, as it hinders effective adhesion to most materials.<sup>95</sup>

Crystallization in semicrystalline polymers leads to a reduction in the specific volume of the polymer, resulting in the generation of residual stress gradients that contribute to warping. When adhesion forces are weak, these stresses cause the part to detach from the build platform.<sup>95,96</sup> Additionally, maximum stresses tend to develop near the edges of the printed part, as each layer attempts to expand during printing because the material properties do not have a good material distribution, but can also be related to the manufacturing process and geometric discontinuities.<sup>97-99</sup> However, the material extrusion process restricts this expansion, leading to the development of stresses that ultimately result in warping.<sup>100</sup> Some studies in the literature suggest the use of fillers to mitigate warping. For example, Winter *et al.* (2022)<sup>101</sup> reported that glass fibers significantly reduced warpage compared with other fillers.

## Conclusions

In conclusion, this study highlights the potential of blending PHBV with P(3HB-*co*-4HB) to enhance or tailor their properties while preserving the fundamental characteristics of the respective PHAs. The FTIR analysis indicated that the structural similarities between the copolymers did not cause band shifts,



suggesting their immiscibility. The tensile test results revealed that adding P(3HB-*co*-4HB) did not significantly affect elongation or reduce the tensile strength or Young's modulus. Nevertheless, the increased 4HB amorphous content in the blends improved impact resistance and raised the energy needed for total fracture.

Dimensional analyses of injection-molded square samples revealed that the blends showed reduced shrinkage, likely including an amorphous phase in the PHBV, which decreased the relaxation time and consequently reduced shrinkage. Additionally, chain alignment led to more pronounced anisotropic shrinkage in the direction of the injection flow.

Thermally, the blends exhibited a relatively high degradation temperature, with no significant changes in the melting or crystallization temperatures, thereby indicating an increased processing temperature window. The overall degree of crystallinity decreased, confirmed mainly by the melting enthalpy reduction with the increase in the P(3HB-*co*-4HB) in the blend.

Soil degradation tests revealed a rapid and complete degradation rate for PX, with blends containing higher P(3HB-*co*-4HB) contents degrading faster due to having the highest content of the amorphous phase. The pure PHBV, with the highest crystallinity, also revealed great biodegradation; however, this was mostly due to its low thickness. In 3D-printing analyses, the optimal processing temperature was found to be slightly above the melting point. Blends with a higher percentage of P(3HB-*co*-4HB) facilitate better extrusion and reduce defects such as warping.

Overall, the study concludes that blends of PHBV and P(3HB-*co*-4HB) enhance material properties and reduce imperfections without the need for additional additives while preserving the intrinsic identity of the PHAs. These blends have significant potential for a variety of applications, including packaging and agriculture, as they expand processing options such as extrusion, thermoforming, and injection moulding. The addition of tailored biodegradability could allow for more controlled degradation in soil, extending the functional lifetime of mulch films and offering a promising alternative to fossil-based and non-degradable polymers.

## Data availability

The data supporting this article have been included as part of the ESI.†

## Author contributions

The manuscript was written through the contributions of all authors.

## Conflicts of interest

There are no conflicts to declare.

## Acknowledgements

This project was supported by Greenwise Campus, Regio Deals, the Province of Drenthe, and the Municipality of Emmen. The authors thank Tobias van der Most



for helping with the processing and mechanical tests and Jur van Dijken for the thermal tests, Ties van der Veen for laboratory assistance, and Ruud Rouleaux from Helian Polymers for the availability in discussing the blends purchased.

## Notes and references

- 1 J. G. Rosenboom, R. Langer and G. Traverso, *Nat. Rev. Mater.*, 2022, **7**, 117–137.
- 2 H. Zhou, R. Bhattacharai, Y. Li, B. Si, X. Dong, T. Wang and Z. Yao, *Sci. Total Environ.*, 2022, **804**, 149985.
- 3 M. Zhang, F. Zhang, C. Li, H. An, T. Wan and P. Zhang, *Polymers*, 2022, **14**, 958.
- 4 J. Shen, J. Liang, X. Lin, H. Lin, J. Yu and S. Wang, *Polymers*, 2022, **14**, 82.
- 5 Z. Terzopoulou, A. Zamboulis, I. Koumentakou, G. Michailidou, M. J. Noordam and D. N. Bikiaris, *Biomacromolecules*, 2022, **23**, 1841–1863.
- 6 M. Zhang, G. M. Biesold, W. Choi, J. Yu, Y. Deng, C. Silvestre and Z. Lin, *Mater. Today*, 2022, **53**, 134–161.
- 7 L. Kaniuk and U. Stachewicz, *ACS Biomater. Sci. Eng.*, 2021, **7**, 5339–5362.
- 8 G. Policastro, A. Panico and M. Fabbricino, *Rev. Environ. Sci. Bio/Technol.*, 2021, **20**, 479–513.
- 9 R. W. Brown, D. R. Chadwick, H. Zang, M. Graf, X. Liu, K. Wang, L. M. Greenfield and D. L. Jones, *J. Hazard. Mater.*, 2023, **441**, 129959.
- 10 A. Raucci, A. Miglione, L. Lenzi, P. Fabbri, J. Di Tocco, C. Massaroni, D. Lo Presti, E. Schena, V. Pifferi, L. Falciola, W. Aidli, C. Di Natale, P. A. Netti, S. L. Woo, D. Morselli and S. Cinti, *Sens. Actuators, B*, 2023, **379**, 133178.
- 11 A. K. Pal, M. Misra and A. K. Mohanty, *Int. J. Biol. Macromol.*, 2023, **229**, 1009–1022.
- 12 A. Pospisilova, J. Vodicka, M. Trudicova, Z. Juglova, J. Smilek, P. Mencik, J. Masilko, E. Slaninova, V. Melcova, M. Kalina, S. Obruca and P. Sedlacek, *Polymers*, 2022, **14**, 2007.
- 13 R. Crétois, N. Follain, E. Dargent, J. Soulestin, S. Bourbigot, S. Marais and L. Lebrun, *Phys. Chem. Chem. Phys.*, 2015, **17**, 11313–11323.
- 14 J. Vodicka, M. Wikarska, M. Trudicova, Z. Juglova, A. Pospisilova, M. Kalina, E. Slaninova, S. Obruca and P. Sedlacek, *Polymers*, 2022, **14**, 1990.
- 15 M. E. Grigore, R. M. Grigorescu, L. Iancu, R.-M. Ion, C. Zaharia and E. R. Andrei, *J. Biomater. Sci., Polym. Ed.*, 2019, **30**, 695–712.
- 16 T. Volova, E. Kiselev, I. Nemtsev, A. Lukyanenko, A. Sukovaty, A. Kuzmin, G. Ryltseva and E. Shishatskaya, *Int. J. Biol. Macromol.*, 2021, **182**, 98–114.
- 17 K.-H. Huong, M. J. Azuraini, N. A. Aziz and A.-A. A. Amirul, *J. Biosci. Bioeng.*, 2017, **124**, 76–83.
- 18 M. Eesaee, P. Ghassemi, D. D. Nguyen, S. Thomas, S. Elkoun and P. Nguyen-Tri, *Biochem. Eng. J.*, 2022, **187**, 108588.
- 19 M. S. Popa, A. N. Frone and D. M. Panaiteescu, *Int. J. Biol. Macromol.*, 2022, **207**, 263–277.
- 20 A. Kościuszko, D. Marciniak and D. Sykutera, *Materials*, 2020, **14**, 22.
- 21 N. A. F. Othman, S. Selambakkannu and N. Seko, *Energy Nexus*, 2022, **8**, 100137.
- 22 W. Chanasit, M. Martla and K. Umsakul, *IOP Conf. Ser.: Earth Environ. Sci.*, 2023, **1139**, 012006.



23 M. Fernandes, A. Salvador, M. M. Alves and A. A. Vicente, *Polym. Degrad. Stab.*, 2020, **182**, 109408.

24 K. C. C. de Carvalho Benini, H. L. Ornaghi, N. M. de Medeiros, P. H. F. Pereira and M. O. H. Cioffi, *Cellulose*, 2020, **27**, 7503–7522.

25 Thingiverse, <https://www.thingiverse.com/thing:2729076#Referencesandtutorials>, accessed 6 March 2023.

26 K. C. C. de Carvalho Benini, H. L. Ornaghi, N. M. de Medeiros, P. H. F. Pereira and M. O. H. Cioffi, *Cellulose*, 2020, **27**, 7503–7522.

27 P. Menčík, R. Příkryl, Š. Krobot, V. Melčová, S. Kontárová, R. Plavec, J. Bočkaj, V. Horváth and P. Alexy, *Int. J. Mol. Sci.*, 2022, **23**, 14409.

28 R. Bellache, D. Hammiche, A. Bettache and A. Boukerrou, *Mater. Today: Proc.*, 2022, **53**, 113–116.

29 L. Hassaini, M. Kaci, N. Dehouche and S. Bruzaud, *Macromol. Symp.*, 2022, **404**, 2100353.

30 P. Feijoo, A. K. Mohanty, A. Rodriguez-Uribe, J. Gámez-Pérez, L. Cabedo and M. Misra, *Int. J. Biol. Macromol.*, 2023, **225**, 1291–1305.

31 Y. Zhou, E. Katsou and M. Fan, *Int. J. Biol. Macromol.*, 2021, **179**, 550–556.

32 M. J. Azuraini, S. Vigneswari, K.-H. Huong, W. M. Khairul, A. K. H. P. S., S. Ramakrishna and A.-A. A. Amirul, *Polymers*, 2022, **14**, 1710.

33 Y. T. Ong, T.-M. Chen and T.-M. Don, *Int. J. Biol. Macromol.*, 2023, **253**, 127001.

34 C. Aversa, M. Barletta and N. Koca, *J. Appl. Polym. Sci.*, 2023, **140**, e53669.

35 X. Wang, Z. Chen, X. Chen, J. Pan and K. Xu, *J. Appl. Polym. Sci.*, 2010, **117**, 838–848.

36 H. Peshne and B. K. Satapathy, *J. Polym. Res.*, 2022, **29**, 496.

37 G. Al, D. Aydemir and E. Altuntaş, *Int. J. Biol. Macromol.*, 2024, **264**, 130745.

38 K. W. Meereboer, K. W. Meereboer, A. K. Pal, M. Misra, M. Misra, A. K. Mohanty and A. K. Mohanty, *ACS Omega*, 2020, **5**, 14221–14231.

39 M. T. Schmid, E. Sykacek, K. O'Connor, M. Omann, N. Mundigler and M. Neureiter, *J. Appl. Polym. Sci.*, 2022, **139**, 51503.

40 R. Bellache, D. Hammiche and A. Boukerrou, *Macromol. Symp.*, 2022, **404**, 2100419.

41 A. Rodriguez-Uribe, T. Wang, A. K. Pal, F. Wu, A. K. Mohanty and M. Misra, *Compos., Part C: Open Access*, 2021, **6**, 100201.

42 M. J. John, *Curr. Res. Green Sustainable Chem.*, 2022, **5**, 100319.

43 T. Omura, T. Goto, A. Maehara, S. Kimura, H. Abe and T. Iwata, *Polym. Degrad. Stab.*, 2021, **183**, 109460.

44 L. Han, C. Han, W. Cao, X. Wang, J. Bian and L. Dong, *Polym. Eng. Sci.*, 2012, **52**, 250–258.

45 A. Kovalcik, J. Smilek, M. Machovsky, M. Kalina, V. Enev, H. Dugova, N. Cernekova, M. Kovacova and Z. Spitalsky, *Int. J. Biol. Macromol.*, 2021, **183**, 880–889.

46 P. Feijoo, K. Samaniego-Aguilar, E. Sánchez-Safont, S. Torres-Giner, J. M. Lagaron, J. Gamez-Perez and L. Cabedo, *Polymers*, 2022, **14**, 2527.

47 R. Luo, K. Xu and G. Chen, *J. Appl. Polym. Sci.*, 2007, **105**, 3402–3408.

48 C. M. Chan, L.-J. Vandi, S. Pratt, P. Halley, Y. Ma, G.-Q. Chen, D. Richardson, A. Werker and B. Laycock, *Composites, Part A*, 2019, **124**, 105437.

49 J. Zhang, X. Lu and T. Chu, *Adv. Mater. Res.*, 2011, **380**, 168–172.

50 L. N. Carli, J. S. Crespo and R. S. Mauler, *Composites, Part A*, 2011, **42**, 1601–1608.

51 V. Venezia, C. Prieto, Z. Evtoski, C. Marcoaldi, B. Silvestri, G. Vitiello, G. Luciani and J. M. Lagaron, *J. Ind. Eng. Chem.*, 2023, **124**, 510–522.

52 P. Feijoo, A. K. Mohanty, A. Rodriguez-Uribe, J. Gámez-Pérez, L. Cabedo and M. Misra, *Int. J. Biol. Macromol.*, 2023, **225**, 1291–1305.

53 M. K. Alqadi, H. M. Al-Khateeb, F. Y. Alzoubi and A. B. Migdadi, *J. Inorg. Organomet. Polym. Mater.*, 2025, **35**, 1281–1291.

54 A. Lagazzo, C. Moliner, B. Bosio, R. Botter and E. Arato, *Polymers*, 2019, **11**, 1477.

55 Z. Li, C. Reimer, T. Wang, A. K. Mohanty and M. Misra, *Polymers*, 2020, **12**, 1300.

56 H. Peshne and B. K. Satapathy, *J. Polym. Res.*, 2022, **29**, 496.

57 J. M. Chai, T. S. M. Amelia, G. K. Mouriya, K. Bhubalan, A.-A. A. Amirul, S. Vigneswari and S. Ramakrishna, *Polymers*, 2020, **13**, 51.

58 B. Meléndez-Rodríguez, S. Torres-Giner, M. A. M. Reis, F. Silva, M. Matos, L. Cabedo and J. M. Lagarón, *Polymers*, 2021, **13**, 1155.

59 X. Li, C. Zhu, H. Wang, Y. Xiao, X. Lu, Y. Li, Z. Liu, Y. Tong and J. Qu, *Polym. Test.*, 2022, **114**, 107700.

60 M. Jo, Y. Jang, E. Lee, S. Shin and H.-J. Kang, *Polymers*, 2022, **14**, 1725.

61 D. Nagy and Z. Weltsch, *Materials*, 2023, **16**, 6402.

62 M. Lay, N. L. N. Thajudin, Z. A. A. Hamid, A. Rusli, M. K. Abdullah and R. K. Shuib, *Composites, Part B*, 2019, **176**, 107341.

63 T. A. Lin, J.-H. Lin and L. Bao, *J. Mater. Res. Technol.*, 2020, **9**, 5304–5312.

64 R. U. Arinze, E. Oramah, E. C. Chukwuma, N. H. Okoye and P. U. Chris-Okafor, *Curr. Res. Green Sustainable Chem.*, 2022, **5**, 100344.

65 N. T.-H. Pham and V.-T. Nguyen, *Adv. Mater. Sci. Eng.*, 2020, **2020**, 8890551.

66 H. Wu, S. Lv, Y. He and J.-P. Qu, *Polym. Test.*, 2019, **77**, 105882.

67 L. Han, C. Han, H. Zhang, S. Chen and L. Dong, *Polym. Compos.*, 2012, **33**, 850–859.

68 V. Ferrão, G. Bortoloni Perin and M. I. Felisberti, *J. Appl. Polym. Sci.*, 2022, **139**, 52782.

69 L. N. Carli, T. S. Daitx, G. P. O. Gonçalves, O. Bianchi, J. S. Crespo and R. S. Mauler, *Polym. Eng. Sci.*, 2020, **60**, 2945–2957.

70 J. Rydz, J. Włodarczyk, J. Gonzalez Ausejo, M. Musioł, W. Sikorska, M. Sobota, A. Hercog, K. Duale and H. Janeczek, *Materials*, 2020, **13**, 2005.

71 M. Abasalizadeh, R. Hasanzadeh, Z. Mohamadian, T. Azdast and M. Rostami, *Iran. J. Mater. Sci. Eng.*, 2018, **15**, 41–51.

72 J. Sun, X. Liao, A. M. Minor, N. P. Balsara and R. N. Zuckermann, *J. Am. Chem. Soc.*, 2014, **136**, 14990–14997.

73 T. Takayama and R. Shibasaki, *Polymers*, 2023, **15**, 4167.

74 K. Iggui, N. Le Moigne, M. Kaci, S. Cambe, J.-R. Degorce-Dumas and A. Bergeret, *Polym. Degrad. Stab.*, 2015, **119**, 77–86.

75 M. Salomez, M. George, P. Fabre, F. Touchaleaume, G. Cesar, A. Lajarrige and E. Gastaldi, *Polym. Degrad. Stab.*, 2019, **167**, 102–113.

76 G. David, J. Michel, E. Gastaldi, N. Gontard and H. Angellier-Coussy, *Int. J. Mol. Sci.*, 2019, **21**, 228.

77 S. Lammi, E. Gastaldi, F. Gaubiac and H. Angellier-Coussy, *Polym. Degrad. Stab.*, 2019, **166**, 325–333.



78 P. Brdlík, M. Borůvka, L. Běhálek and P. Lenfeld, *Polymers*, 2022, **14**, 838.

79 C. M. Chan, L.-J. Vandi, S. Pratt, P. Halley, D. Richardson, A. Werker and B. Laycock, *Sustainable Mater. Technol.*, 2019, **21**, e00099.

80 D. C. Hall, P. Palmer, H.-F. Ji, G. D. Ehrlich and J. E. Król, *Front. Microbiol.*, 2021, **12**, 646303.

81 N. Khaki, E. Sharifi, M. Solati-hashjin and N. Abolfathi, *J. Biomater. Appl.*, 2025, **39**, 734–747.

82 P. Feijoo, A. Marín, K. Samaniego-Aguilar, E. Sánchez-Safont, J. M. Lagarón, J. Gámez-Pérez and L. Cabedo, *Polymers*, 2023, **15**, 2481.

83 X. Wen and X. Lu, *J. Polym. Environ.*, 2012, **20**, 381–387.

84 T. G. Volova, S. V. Prudnikova, O. N. Vinogradova, D. A. Syrvacheva and E. I. Shishatskaya, *Microb. Ecol.*, 2017, **73**, 353–367.

85 S. Zainuddin, S. M. Kamrul Hasan, D. Loeven and M. Hosur, *J. Polym. Environ.*, 2019, **27**, 2292–2304.

86 S. Muniyasamy, O. Ofosu, B. Thulasinathan, A. S. Thondi Rajan, S. M. Ramu, S. Soorangkattan, J. B. Muthuramalingam and A. Alagarsamy, *Biocatal. Agric. Biotechnol.*, 2019, **22**, 101394.

87 Z. Zaidi, D. Mawadand and A. Crosky, *Front. Mater.*, 2019, DOI: [10.3389/fmats.2019.00275](https://doi.org/10.3389/fmats.2019.00275).

88 S. Wang, P. Ma, R. Wang, S. Wang, Y. Zhang and Y. Zhang, *Polym. Degrad. Stab.*, 2008, **93**, 1364–1369.

89 A. W. Ajmal, F. Masood and T. Yasin, *Appl. Clay Sci.*, 2018, **156**, 11–19.

90 S. Kontárová, R. Přikryl, V. Melčová, P. Menčík, M. Horálek, S. Figalla, R. Plavec, J. Feranc, J. Sadílek and A. Pospíšilová, *Materials*, 2020, **13**, 4736.

91 V. Melčová, K. Svoradová, P. Menčík, S. Kontárová, M. Rampichová, V. Hedvíčáková, V. Sovková, R. Přikryl and L. Vojtová, *Polymers*, 2020, **12**, 2806.

92 J.-W. Tseng, C.-Y. Liu, Y.-K. Yen, J. Belkner, T. Bremicker, B. H. Liu, T.-J. Sun and A.-B. Wang, *Mater. Des.*, 2018, **140**, 209–221.

93 W. Kanabenza, N. Passornraprasit, C. Aumnate, T. A. Osswald, D. Aht-Ong and P. Potiyaraj, *Addit. Manuf.*, 2024, **86**, 104205.

94 M. V. Candal, I. Calafel, M. Fernández, N. Aranburu, R. H. Aguirresarobe, G. Gerrica-Echevarria, A. Santamaría and A. J. Müller, *Polymer*, 2021, **224**, 123734.

95 N. Bachhar, A. Gudadhe, A. Kumar, P. Andrade and G. Kumaraswamy, *Bull. Mater. Sci.*, 2020, **43**, 171.

96 M. Spoerk, C. Holzer and J. Gonzalez-Gutierrez, *J. Appl. Polym. Sci.*, 2020, **137**, 48545.

97 A. Kelly, E. Phillips, A. A. Vijayachandran and A. Waas, in *AIAA SCITECH 2024 Forum*, American Institute of Aeronautics and Astronautics, Reston, Virginia, 2024.

98 M. Shendy, M. Alkhader and B. A. Abu-Nabah, in *2022 Advances in Science and Engineering Technology International Conferences (ASET)*, IEEE, 2022, pp. 1–4.

99 K. M. Panchasara, A. N. Ramakrishnan, K. Mehle, C. Ludtka and S. Schwan, *Macromol. Symp.*, 2022, **403**, 2100465.

100 M. N. Jahangir, K. M. M. Billah, Y. Lin, D. A. Roberson, R. B. Wicker and D. Espalin, *Addit. Manuf.*, 2019, **28**, 354–364.

101 K. Winter, J. Wilfert, B. Häupler, J. Erlmann and V. Altstädt, *Macromol. Mater. Eng.*, 2022, **307**, 2100528.

